Edinburgh Research Explorer

Imaging vertical interfaces using acoustic time reversal

OPEN ACCESS

Imaging vertical interfaces using acoustic time-reversal

Satyan Singh[*] **and Andrew Curtis**[*]

[*]*University of Edinburgh,*

Department of Geosciences,

Edinburgh Interferometry Project,

Email: s.singh@ed.ac.uk

(December 16, 2018)

Running head: **Imaging Vertical Interfaces**

————

ABSTRACT

We present a novel approach to image vertical structures using multiply scattered waves. This method require only a smooth seismic velocity model and data recorded at the surface. Previous methods to image near-vertical interfaces or faults using migration methods all require prior information about small-scale details in the seismic velocity model in order to infer the locations of multiple-scattering wave interactions. We use waves that have their last scattering interaction with near-vertical interfaces, while their other scattering points may be anywhere in the Earth, including at the free surface. Our algorithm then images the final scattering point using a time-reversed mirror-style imaging condition, so we refer to the method as Time-Reversed Mirror imaging (TRMi). Artifacts in the images produced have clear causes and can be filtered out by stacking over shots and including contributions from multiples. Our numerical examples demonstrate the successful application of the method for staircase structures and a section of the Marmousi model. They also reveal a new way to diagnose errors in the smooth or reference velocity model used. In addition, our method can be used to image point scatterers in active seismic surveys, or for event location in passive surveys.

INTRODUCTION

Traditional wavefield imaging methods such as Kirchhoff migration (Wiggins, 1984), reverse time migration (Baysal et al., 1983; McMechan, 1989; Whitmore, 1983), and downward continuation algorithms (Claerbout, 1985) assume the first-order Born approximation —that each wave is scattered no more than once (like event i in Figure 1(a)). They all require knowledge of a smooth model of the medium's velocity (a macro-velocity model) within which the unknown scatterers are assumed to be embedded. Since only singly scattered recorded waves or events (often called primaries) contribute correctly to images within such algorithms, it is unlikely that near-vertical structures can be imaged unless very long offset data are available. This is because any wave from the source that reflects off near-vertical structures will generally be propagating downwards after reflection, making it difficult to record at the surface (event ii in Figure 1(a)). Given a sufficient velocity gradient with

depth, it is possible that such waves eventually bend back to the surface (at which point they are referred to as diving waves, e.g., Figure 1(b)). While it is true that diving waves can be used to image vertical structures under the Born approximation (Xu and Jin, 2006), sufficiently long offsets are often not available to record such waves, and a very good macro-velocity model is required to correctly position reflectors due to the length of the curved wave path that must be predicted correctly by that model. Such an accurate model is often unavailable. If a Vertical Seismic Profile (VSP) has recorded the reflections from the vertical interface then we can use those recordings to image the structure using reverse-time migration (RTM) or interferometric imaging (Hornby and Yu, 2007), but of course VSP measurements are only available near boreholes.

[Figure 1 about here.]

If prior information is available about abrupt interfaces in the velocity model, we can predict waves that are up-coming from the subsurface interface at which they reflect or scatter. These upcoming waves may then reflect a second time from vertical interfaces (called duplex or doubly-scattered waves) before being recorded (Figure 1(c)). Marmalyevskyy et al. (2005) and Jin et al. (2006) show that we can then use these waves to image the vertical interfaces using RTM. Malcolm et al. (2009) followed a similar approach to Jin et al. (2006) but inverted for the abrupt interfaces in the velocity model starting from a smooth version of the velocity prior to imaging. These doubly-scattered waves are also called prismatic waves and have been used extensively to image salt flanks and narrow mini-basin areas (predominantly vertical interfaces) once we have the prior location of at least one reflecting interface (Farmer et al., 2006; Zhang and Sun, 2009; Cavalca and Lailly, 2005; Liu et al., 2011; Li et al., 2011). However, obtaining a smooth version of the velocity model is a far simpler task than obtaining accurate estimates of abrupt, reflecting interfaces in the model (Noble et al., 1991; Symes and Carazzone, 1991; Chavent and Jacewitz, 1995; Sava and Biondi, 2004). Hence, a more direct method to produce images from up-going waves without such prior information is desirable.

Recently, Marchenko-type algorithms were developed that estimate the Green's func-

tions from surface sources to any subsurface point that includes all primaries and multiple reflections using only smooth velocity models (Rose, 2002; Broggini et al., 2012; Wapenaar et al., 2014; Singh et al., 2014; da Costa Filho et al., 2014; Singh and Snieder, 2017). However, these methods fail to image vertical interfaces because Marchenko imaging is based on the kinematic similarity of the up- and down-going Green's function at the interface (Lomas et al., 2018). At a vertical interface, the up- and down- going Green's function would not be similar as shown in Figure 1d, leading to failure of the Marchenko-imaging method. Lomas et al. (2018) demonstrate that using modified Marchenko-type equations and VSP recordings they can retrieve the Green's functions between the vertical interfaces and the surface; they then apply an interferometric imaging condition to image the vertical interface with these Green's functions. However, again, this can only be achieved in the vicinity of a borehole.

Zuberi and Alkhalifah (2014) used a smooth velocity model to image vertical interfaces using a technique called generalized internal multiple imaging (GIMI). GIMI uses successive crosscorrelations with the surface recorded data and its back-propagated version to enhance different orders of scattering, and then uses these crosscorrelations for imaging in an RTM-type procedure. Although this scheme uses specific orders of internal multiples to construct parts of the model that are not imaged by primaries, it also produces imaging artifacts.

We take a different approach to all of the studies above: we image the vertical structures using all orders of multiply scattered waves (including free-surface multiples) with reduced imaging artifacts, using only a smooth version of the velocity model, without the need for a density model and without knowledge of the source time-function or wavelet. This is achieved by applying a novel imaging condition to the full recorded wavefield. Time-reversed modeling is the starting point of our imaging method (Fink, 1999) and is related to passive source-location methods of Larmat et al. (2006), Artman et al. (2010), and Zhebel et al. (2011). However, we cast these ideas in a RTM framework (using active sources), and use them to image vertical interfaces. The ability to image such interfaces differentiates our work from that of Shustak and Landa (2018) who used time reversal for scatterer detection from active sources and event location for passive sources.

We achieve this by time reversing the recorded data, backpropagating it to construct a subsurface wavefield in the smooth reference model, and then passing this wavefield to an imaging condition. Thus, the receivers (at the acquisition surface) act as a time-reversal mirror (Fink, 1992, 2008), hence we refer to this imaging technique as Time-Reversed Mirror imaging (TRMi).

The principle difference to RTM methods is that the source field is never simulated or extrapolated into the subsurface. Key to the method is that the latter difference allows all orders of scattering waves to contribute to the image, despite the smooth velocity model. Below, we first introduce the imaging condition applied to the receiver wavefield, then present numerical examples which include a structurally complex synthetic medium: the Marmousi model. Finally, we discuss the elastic extension of our algorithm.

THEORY

With a smooth velocity model, Reverse-Time Migration (RTM) images the subsurface at interfaces that can be interrogated using recorded singly scattered waves. This is achieved by first predicting what the injected source wavefield must have looked like in the subsurface after the source was fired, and what the recorded wavefield must have looked like in the subsurface before it was recorded at receivers. The source wavefield is created by injecting the known source wavelet into a computational wavefield propagator (in our case a finite-difference solution to the wave equation) through the reference velocity model: predicts where that source energy will have gone in the subsurface as a function of time, and we denote this wavefield $U_s(\mathbf{x}, t)$. The receiver-side wavefield is created by injecting the time-reverse of the data recorded at the surface into a computational wavefield propagator at the receiver locations; since the wave equation is the same whether the waves propagate forwards or backwards in time, this propagated wavefield emulates the recorded wavefield moving backwards in time into the subsurface, and we denote this wavefield $U_r(\mathbf{x}, t)$.

Intuitively then, the source wavefield is the wavefield in the background medium that goes forward in time from the source time t_0 to the maximum recording time T, while the receiver wavefield takes the recorded data backward in time from T to t_0. If we play both

5

the source and receiver wavefields forwards from t_0 to T, singly-scattered waves in both the source and receiver wavefields will overlap each other at each interface, since the source wavefield created the singly-scattered receiver wavefield at those locations. Therefore, in the second step of RTM we applying an appropriate *imaging condition* which measures the similarity of source and receiver wavefields at each point in the subsurface model. The most common condition is the zero-lag crosscorrelation of wavefield $U_s(\mathbf{x}, t)$ and $U_r(\mathbf{x}, t)$.

The key assumption in RTM is that these wavefields are most similar at the locations of reflectors so that the zero-lag of the crosscorrelation should be maximum at such locations. Since this would be true at consistent locations for every shot (assuming reflectors are static), the zero-lag crosscorrelations are calculated everywhere across the image and summed over all shots. This leads to the so-called RTM imaging condition (Claerbout, 1985):

$$R(\mathbf{x}) = \sum_{shots} \sum_{t=t_0}^{T} U_s(\mathbf{x}, t) U_r(\mathbf{x}, t), \tag{1}$$

where the zero-lag crosscorrelation is equivalent to a summation of the product of our two wavefields for all recording times t, for $t \in (t_0, T)$.

For multiply scattered waves, the path to the *first* scattering point from the source in U_s is correct, while in U_r only the path from the *last* scattering point to the receiver is correct; all other paths (between remaining scattering points) in both fields are not correctly predicted with the assumption of the smooth reference model. Consequently, if the first and last scattering points are not identical (i.e, if the wave is not a primary), then U_r and U_s will not overlap at the scatterer so the zero-lag crosscorrelation (the image) will be relatively small at this point and the scatterer will not be imaged. Unfortunately, this same energy in U_s and U_r may overlap at a different location (not corresponding to a scatterer) because of the errors in their wave paths and this leads to imaging artifacts.

Vertical interfaces can usually only be interrogated by body waves that scatter a minimum of twice in the subsurface. Figure 1(c) shows that in this case we can only reconstruct the source wavefield by including the abrupt interface (solid line) in the reference model. Therefore, RTM would not be able to create an image using these multiply scattered waves in a smooth reference model.

However, notice that in Figure 2(a) both the primary and duplex waves are coincident in space and time at the vertical interface, and both events can be predicted at that point from the *recorded* wavefield using only the *smooth reference model*. We use this notion to develop our imaging algorithm: replacing the source wavefield with the receiver wavefield in equation 1, we re-trace the paths taken by primary and duplex waves in Figure 2(a): these waves overlap only at the vertical interface. To highlight this overlap, we apply a 2D Laplacian operator to the image. The Laplacian operator is a high-pass filter that is commonly used in image processing (Pratt, 2013); when applied to our wavefields, it highlights the locations of overlap of waves, which is at the vertical structure for the primary and duplex wave. The key aspect of this argument is that it applies to wave paths with any order of scattering that interact last with the vertical interface. As shown in Figure 2(b), time reversal will still focus transmitted and scattering energy on the vertical interface for a free-surface multiple (solid rays) or an internal multiple (dashed rays).

If we only replace U_s with U_r in equation 1, without the Laplacian operator, we obtain images that are masked by low-wavenumber artifacts (see below). These are similar to the low-wavenumber artifacts observed in RTM when reflective interfaces are included in the reference model (Guitton et al., 2006; Zhang and Sun, 2009), which are typically also removed by applying the Laplacian operator. The Laplacian highlights areas of the image that vary more rapidly in lateral or vertical directions that do surrounding areas.

For a single shot, waves frequently overlap each other by chance when they are not necessarily at an interface, which also contributes to the image. Fortunately most of the overlapping events that are not along interfaces are not coherent from shot to shot, while the scattered and primary waves shown Figure 2(a) are coherent between shots. Consequently, summing over all shots reduces these non-coherent artifacts while enhancing true reflectors. Our final imaging condition becomes:

$$I(\mathbf{x}) = \nabla_{\mathbf{x}}{}^2 \sum_{shots} \sum_{T} U_r(\mathbf{x}, t) U_r(\mathbf{x}, t), \tag{2}$$

where $\nabla_{\mathbf{x}}{}^2$ is the 2D Laplacian operator for 2D imaging and the 3D Laplacian operator for 3D imaging. For simplicity we refer to this method as Time-Reversed Mirror imaging (TRMi). In principle, the summation over time for TRMi is for $t \in [\bar{t}_0, T]$ where $\bar{t}_0$ is $-\infty$

and T is the maximum recording time. For practical purposes, $\bar{t}_0$ can be a few seconds before the source time, and such details are explained in our numerical examples section.

Note that the receiver wavefield U_r used in TRMi is the same as the receiver wavefield used in RTM imaging. Thus no additional modeling is required in order to apply the new method. Nevertheless, the imaging condition in equation 2 is quite different from RTM in equation 1. First, equation 2 does not involve the source field U_s at all. Since both fields U_r on the right of equation 2 are identical, the operation within the summation is a zero-time autocorrelation. This leads to substantially different images as we show below. Since RTM tends to image horizontal structures and TRMi tends to image vertical structures, we also create a final image that is the sum of the two: Image = RTM + TRMi. This will be shown for each of the examples that follow.

[Figure 2 about here.]

NUMERICAL EXAMPLES

We test our imaging condition by applying it to models that include vertical interfaces and faults, in both step models and modified versions of the Marmousi model (Versteeg, 1994). Note that we removed the direct arrivals from the recorded data before using them for TRMi, as these arrivals do not scatter and hence do not conform to the assumption of our imaging condition. In all numerical examples the sources and receivers are at the top surface of the model.

Step Model

To introduce various properties of TRMi: we use a simple synthetic step-model that includes a single vertical interface as shown in Figure 2(a). The model has a transparent acquisition surface to simplify wavefields by removing free-surface multiples (we discuss free-surface multiples below), and the step structure is created by density contrasts with a constant seismic velocity of 2 km/s across the model so that rays are straight between reflection

points. This merely enables a more straightforward interpretation of wavefields, and we show below that constant velocity is not required by the method.

In the step model examples, there are 501 sources and receivers at the surface with a spacing of 4 m, starting at -1.0 km. Our recorded data consist of primaries (from the horizontal interfaces), diffractions (from the top and bottom of the step at 0 km laterally), and duplex waves (waves that scatter twice in the subsurface, once from the horizontal interface at 0.9 km and once from the vertical interface).

The associated Reverse Time Migration (RTM) image of this step model is shown in Figure 3 and was constructed using equation 1 and a reference model that is constant in both density and velocity (i.e., no details of the true subsurface model are included in the reference model). RTM clearly images horizontal interfaces but not the vertical interface. The vertical interface is missing because only duplex waves (scattered twice) reflect from the vertical part of the model (Figure 1 (c)), so standard migration without interfaces included in the reference model can not correctly position energy from multiply scattered waves.

[Figure 3 about here.]

The corresponding TRMi of the step model constructed using equation 2 and only one shot is shown in Figure 4(a). Figure 4(a) images the vertical interface because equation 2 images the points of overlap between the primary reflections from the right-hand horizontal interface (transmitted through the vertical interface) and the duplex waves that are additionally reflected at the vertical interface (illustrated in Figure 2(a)).

[Figure 4 about here.]

This image also includes some artifacts not related to the vertical interface. To understand these artifacts we first look at the time evolution of TRMi for a single shot to the right of the vertical interface at x=1 km. The imaging condition for each of the time-evolving snapshots can be written as $I(\mathbf{x}, \bar{t}_0) = \nabla^2 \sum_{\bar{t}_0}^{T} U_r(\mathbf{x}, t) U_r(\mathbf{x}, t)$, where we now vary the minimum time step $\bar{t}_0$ that is considered in the image. In other words, for each of these time-evolving image snapshots (shown in the right panels of Figure 5), the maximum recording time T in

equation 2 is fixed at 3.0 seconds and the time integral is performed over $[\bar{t}_0, T]$ for different values of $\bar{t}_0$ (staring at 1.2 seconds and decreasing in intervals of 0.12 seconds).

[Figure 5 about here.]

The temporal evolution of the image in Figure 5 allows us to identify which waves overlap in the receiver wavefield (left panels of Figure 5) thus contributing to the image for one shot. By stacking over all shots that include the waves reflecting from the vertical interface (duplex waves), only the coherent parts of the image across all shots survive. These coherent parts of the image (labeled V in Figure 5) derive from the interaction of the duplex wave (labeled D in Figure 5) and the primary (labeled P in Figure 5) at the vertical interface, while the incoherent parts vanish through stacking, as shown in Figure 4(b). The incoherent parts, (labeled $\mathbf{a}'$ and $\mathbf{b}'$ in Figure 5) occur for single shots and are caused by overlapping events that are not at an interface.

Event $\mathbf{a}$ in Figure 5 is an edge artifact that is generated while reconstructing the receiver wavefield. These artifacts are a result of receivers at the ends of the recording array creating secondary waves when injected in our propagator. With an infinitely long array, these waves would destructively cancel with those from the next receiver; hence they are purely a result of using an array of finite aperture, and they are minimized by tapering the amplitudes of the injected data towards either end of the array. Alternatively, we could have implemented the boundaries of our propagator better as explained in Clapp (2009). For this particular shot, event $\mathbf{a}$ overlaps with the primary to create $\mathbf{a}'$ in the image (right panel of Figure 5). Event $\mathbf{b}$ is the diffraction from the top of the step structure; it overlaps with the primary to form $\mathbf{b}'$ in the TRMi image.

We then follow equation 2 and stack similar images over all shots that include the duplex wave. The artifacts are reduced by destructive interference since they are not coherent between shots, as shown in Figure 4(b). Finally, a full image of the subsurface can be constructed by adding the RTM image to the TRMi as illustrated in Figure 6, showing that the step structure can be imaged using only a homogeneous reference model.

Shots that do not include the duplex wave (to the left of the step structure) will not

contribute to imaging the vertical interface as shown in Figure 4(c) for a shot at x=-1 km. This image includes an artifact caused by focusing of the primary wave from the top interface at a depth around 0.8 km. This is twice the actual depth of the interface, or more specifically, it is the depth at the mirror position of the surface source reflected through the subsurface interface. Since the focusing of the primary is not spatially coherent across different shots, this focusing artifact destructively sums in the final TRMi image over all shots as shown in Figure 4(d). Figure 4(c) also includes contributions from the diffraction focusing at the top and base of the vertical structure (at the correct spatial positions at 0.4 km and 0.8 km depth) and an imaging artifact at shallow depths similar to $\mathbf{a}'$ in Figure 5. Even though stacking over shots removes the primary focusing artifacts, artifacts above 0.4 km depth remain in Figure 4(d).

Not including the Laplacian operator as part of the imaging condition in equation 2 results in an image that is masked by low-wavenumber artifacts (see Figure 7) as explained in the Theory section. In this case, the image of the vertical interface is almost completely obscured by these artifacts. Therefore the Laplacian removes these low-wavenumber artifacts and consequently highlights the overlap between the duplex and the primary wave at the vertical interface.

[Figure 6 about here.]

[Figure 7 about here.]

Step Model with free surface

We note that the duplex wave (D) and the primary (P) in Figure 5 overlap exactly on the vertical part of the step as shown in Figure 2(a) and hence construct the image in Figure 4(a). These waves are both a result of a singly scattered event that propagates from the source (star) to the vertical structure via a reflection, illustrated by the solid line in Figure 2(a). As shown in Figure 2(b), this solid line does not need to be singly scattered: it can be any wave, primary or multiple, that meets the interface to create both transmitted and

11

additionally scattered events: both such events will always be correctly migrated back to the vertical structure using the reference velocity model and the TRMi imaging condition.

In a second example, we therefore add a structure that generates multiples. The second model resembles Figure 2(a) except that a free surface is added at 0 km depth. We apply our imaging algorithm in equation 2 to synthetic data from this model including all shots at the surface, yielding the image in Figure 8(a). By including the multiples, more information contributes to the image of the vertical structure and hence we obtain a better image than that created without the multiples in Figure 4(b). Specifically, we obtain fewer artifacts above the vertical structure, so above 0.4 km depth. We also observe a better final image given by RTM + TRMi (with the multiples included in the TRMi) as shown in Figure 8(b) compared to the final image without multiples in Figure 6.

Note that the image at the top of the step (depth 0.4 km) is not an artifact: it is formed by the diffracted waves from the top of the step focusing at their correct location. The same effect occurs at the diffracting corner at the base of the step, at 0.8 km depth, but this is not as obvious due to the relatively low amplitude of this energy compared to the reflected waves. Therefore, we not only image the vertical parts of the model at the correct position using multiply reflected waves (if the reference velocity model is kinematically accurate) but also diffractors are imaged at their correct positions.

[Figure 8 about here.]

Two-step staircase model with additional interfaces

We then increased the number of interfaces and steps in our model as shown in Figure 9. This ensures that there are more overlapping events at locations that do not correspond to interfaces. The corresponding full subsurface image (i.e., the addition of the RTM and TRMi) is shown in Figure 10, successfully displaying the vertical structures although the amplitude of the smaller, right-hand vertical structure is significantly reduced. We note that this smaller step is rather a stringent test of the imaging method since the length of the vertical reflector is 0.09 km which is of the same order as the dominant wavelength of 0.08

12

km. Therefore the reflection from the vertical interface will interfere with the diffraction from the top and bottom corners of the step across its entire length.

This image has minimal artifacts which includes remnants of the free-surface multiple artifacts at depth below each vertical interface. For example, one such artifact remains immediately above and below each step. This is because the duplex and the primary can still overlap at these locations, although their amplitudes are significantly diminished compared to the image along the true vertical structure. Therefore, a shortcoming of TRMi can be that it is difficult to delineate exactly where the boundaries of each vertical interface end.

We modified the model in Figure 9 to include a free surface, with the associated full image given in Figure 11. The additional contributions from the multiples to the image constrain the boundaries of the vertical step better in Figure 11 compared to the case without using free-surface multiples in Figure 10. In this case, even the smaller vertical step is reasonably well imaged.

[Figure 9 about here.]

[Figure 10 about here.]

[Figure 11 about here.]

Marmousi Model

As a more complex test, we compressed a section of the Marmousi model (Versteeg, 1994) by a factor of 4 laterally to create a model with more steeply dipping interfaces, and included a free surface (Figure 12); we call the resulting model the *squeezed Marmousi model*. The acquisition surface is placed 12 m below the free surface and populated with 601 receivers. We model the recorded pressure data using a finite-difference solution to the wave equation (our wavefield propagator), initially with the interfaces defined by density contrasts with a constant velocity of 2 km/s throughout the model. Although, we use

pressure recordings to perform TRMi, we can alternatively use velocity or displacement recordings with similar results. We removed the direct wave from the recordings and used the remaining data to construct the receiver wavefield. This wavefield is constructed using our propagator with a smooth (constant) velocity model (this is our reference model: no details of reflectors in the true model are included). The result of TRMi is shown in Figure 13(b) while the corresponding RTM is shown in Figure 13(a). The major steeply dipping faults in the squeezed Marmousi model (indicated by guidelines consisting of red dots) are better imaged by TRMi. These are imaged because the waves reflecting from these faults have higher amplitudes compared to other near-vertical features in the Marmousi model, as they are the locations of the largest acoustic impedance contrasts in the model (from blue to red in Figure 12). The final RTM + TRMi image of the Marmousi model in Figure 12 is shown in Figure 13(c). This is clearly better than either of the images from RTM or TRMi individually.

We modified the model by creating interfaces in the velocity field instead of density, now keeping the density constant at 2 kg/m^3. Wave paths then bend and the recorded data includes diving waves and refractions. The corresponding TRMi using a smoothed reference velocity model, is shown in Figure 14(b) showing that the major faults are still imaged. Interestingly, we also image a high-impedance interface that is closer to horizontal, shown in yellow on Figure 14(b); this is because of the overlapping of the diving wave transmitted through this interface and its reflected primary (a schematic of these wave paths are shown Figure 15). There are more artifacts in the TRMi in this case due to the overlapping of the diving wave with other events in the time-reversed wavefield. At the edges of the acquisition, the TRMi is not reliable as we taper the edges of the recorded data.

The corresponding RTM and final image are shown in Figures 14(a) and 14(c), respectively. The RTM image in Figure 14(a) images the steeply dipping faults better than the RTM image in Figure 13(a) because of the presence of diving waves, but it still fails to image some of the high-impedance faults. The TRMi image in Figure 14(b) is nevertheless able to image them.

[Figure 12 about here.]

[Figure 13 about here.]

[Figure 14 about here.]

[Figure 15 about here.]

DISCUSSION

Our numerical examples demonstrate that TRMi has the potential to image vertical interfaces if we have recorded both waves that transmit through each point on the interface, and the corresponding duplex or higher-order scattered waves which reflect from the same point on the interface then transmit directly to the receiver array. In the case where one of these waves is not recorded due to receiver coverage or to the nature of the subsurface, the imaging condition fails. In addition our method does not require any knowledge of the source wavelet as we only use the recorded data at the surface and a reference velocity model as inputs.

Duplex waves have two scattering points, the last of which must be on the vertical structure to be imaged. Consequently these waves have lower amplitudes ($O(r^2)$) compared to primary events ($O(r)$), where r is a typical reflection coefficient. Notice that formally the transmitted wave that has interacted with the vertical interface is also a duplex wave since it was forward-scattered by the interface. It therefore has amplitude $O(r(1-r))$. Our proposed TRMi method multiplies U_r with itself (equation 2), so the resulting amplitude of the duplex wave contributions to the image will be $O(r^3(1-r))$. They are therefore expected to have lower amplitudes than those contributing to the RTM, since RTM correlates the source wavefield ($O(1)$) with the primaries $O(r)$. For these reasons we might boost the amplitudes at later times in the recorded data prior to imaging to help to increase the magnitude of the contributions from the duplex waves, noting that inevitably gaining the amplitudes at later times can introduce or increase noise in the recorded data. As an alternative, Meles and Curtis (2014) and Löer et al. (2015) developed algorithms that in

principle are capable of identifying specific orders of diffracted wavefields, and a related method for reflected waves was developed by Meles et al. (2014) and da Costa Filho et al. (2017). Hence, it may be possible in future to identify the multiply scattered waves that correspond to each primary in seismic data, and increase the amplitudes of these waves without boosting the surrounding noise.

TRMi also creates artifacts implicitly: waves that overlap away from any interface can add spurious energy to the image. Since these waves are not coherent from shot to shot while waves that overlap along true interfaces are coherent, stacking over shots suppresses the spurious energy in TRMi but preserves coherent energy at true interfaces. Another artifact is the focusing of single-shot primaries from horizontal layers in the subsurface (at twice the depth of such interfaces if the velocity structure is constant). Again, when we stack over shots these artifacts disappear. In our examples, we also extended the time axis to times before zero. This ensures that waves do not abruptly end in the receiver wavefield at zero time, as this can contribute to the TRMi when we apply the Laplacian operator.

Our method fails to recover the true amplitudes of the subsurface reflectivity, unlike Marchenko imaging algorithms (Wapenaar et al., 2014; Slob et al., 2014; Singh et al., 2015, 2016; Singh and Snieder, 2017), but benefits from imaging vertical interfaces which Marchenko methods fail to do. In theory, Marchenko imaging retrieves the true reflection coefficient by deconvolving the up- and down-going Green's function at every point, whereas in TRMi we do not relate the reflection coefficient to the fields used for imaging. Indeed, since our method has no direct amplitude relationship with methods like Marchenko or RTM it is unclear how to combine the images to get a full image of the subsurface with both horizontal and vertical structures of comparable amplitudes. da Costa Filho and Curtis (2016) have shown how to combine images from different imaging methods (in their example Marchenko imaging and RTM) to obtain a new image with reduced artifacts. However, in the case considered here we cannot apply that method as it is designed to highlight the similarity between images; in our case, the images from RTM and TRMi may not contain similar structures, and in the extreme end-member case when the images are entirely different from each other, the method of da Costa Filho and Curtis (2016) would give a zero

image.

Interestingly, if incorrect kinematics are caused by errors in the migration reference model, there is a discrepancy between the effects on TRMi images and those obtained by other methods. For instance, when the velocity used for migration is too slow, the duplex wave and the transmitted wave both take longer to reach their point of overlap during redatuming, which results in the imaged vertical structures being located *deeper* than their true position. By contrast, for a slow reference model, RTM places the horizontal reflectors at *shallower* positions than their true locations, as the source wavefield and the receiver wavefield overlap at earlier times. This discrepancy in the position of vertical reflectors from our method and horizontal reflectors from RTM is shown in Figure 16 for the step model in Figure 2(a). Images such as Figure 16 may provide a diagnostic to verify whether the reference model used for migration is accurate: it would be possible in this case to vary the velocity until vertical and horizontal interfaces fit together. How to use such an image to update the velocity automatically remains unclear at this point. In addition, Lellouch and Landa (2018) have shown that we can use the degree of focusing of point diffractors from the time-reversal and back propagation of the recorded field to invert for the velocity field. Since our method also relies on both time-reversal and back propagation, Lellouch and Landa (2018) may be another starting point to investigate how to invert for the velocity model.

[Figure 16 about here.]

Although, we do no investigate the elastic extension of the method in detail, we briefly discuss it for completeness. If the elastic recording is separated into P- and S-waves, we can apply our algorithm to each of these datasets (the separated P-waves or the separated S-waves) individually to image the vertical interfaces since these will also conform to similar ray geometries to those of Figure 2(a). In addition, we can potentially crosscorrelate the P- and S-wavefields with each other to image all interfaces as both P- and S-waves meet at any interface that caused P-to-S or S-to-P conversions, regardless of the dip of each interface. This approach of using both the P- and S-wave for imaging is similar to the

work of Van Manen (2006, Chapter 4) and Galetti and Curtis (2012), as effectively the crosscorrelation is one form of a so-called receiver function. Removing the focusing artifacts as discussed in the previous paragraph will no longer be trivial, as useful contributions to the image then occur for all dips. Nevertheless, if our objective is to identify vertical interfaces, we might still filter out the non-vertical interfaces in the image even though some of these non-vertical interfaces in the image may not be artifacts.

To apply the methods developed herein to real data, we have to make an acoustic approximation. There will be no need to invert for the source time-function but we still need a reference velocity model. There is also no need for additional wavefield extrapolations if RTM is also applied (as is standard in many applications). The method therefore offers a relatively cheap addition to standard imaging methods.

CONCLUSION

We show that near-vertical structures can be imaged using multiply scattered waves using Time-Reversed Mirror imaging (TRMi). The waves that contribute have their last scattering point on the vertical structure, while their other scattering point or points can be anywhere in the medium. TRMi is complimentary to reverse-time migration: when used simultaneously, it can also be used to indicate errors in the migration velocity model and can be applied at relatively low additional computational cost. Significantly, our proposed method only requires a smooth reference model to image the near-vertical structures using multiply-scattered waves. In fact, the more multiple scattering from the vertical structures in our recorded data, the better the chance to image these structures, as we show in our numerical staircase examples and in the Marmousi model. Our algorithm has the additional advantage of correctly imaging diffraction locations, and interfaces which have overlapping diving waves and primaries, as occurs in our test using the Marmousi model.

REFERENCES

Artman, B., I. Podladtchikov, and B. Witten, 2010, Source location using time-reverse imaging: Geophysical Prospecting, **58**, 861–873.

Baysal, E., D. D. Kosloff, and J. W. Sherwood, 1983, Reverse time migration: Geophysics, **48**, 1514–1524.

Broggini, F., R. Snieder, and K. Wapenaar, 2012, Focusing the wavefield inside an unknown 1D medium: Beyond seismic interferometry: Geophysics, **77(5)**, A25–A28.

Cavalca, M., and P. Lailly, 2005, Prismatic reflections for the delineation of salt bodies, *in* SEG Technical Program Expanded Abstracts 2005: Society of Exploration Geophysicists, 2550–2553.

Chavent, G., and C. A. Jacewitz, 1995, Determination of background velocities by multiple migration fitting: Geophysics, **60**, 476–490.

Claerbout, J., 1985, Imaging the Earth's interior: Blackwell scientific publications.

Clapp, R. G., 2009, Reverse time migration with random boundaries, *in* SEG technical program expanded abstracts 2009: Society of Exploration Geophysicists, 2809–2813.

da Costa Filho, C. A., and A. Curtis, 2016, Attenuating multiple-related imaging artifacts using combined imaging conditions: Geophysics, **81**, S469–S475.

da Costa Filho, C. A., G. A. Meles, and A. Curtis, 2017, Elastic internal multiple analysis and attenuation using marchenko and interferometric methods: Geophysics, **82**, Q1–Q12.

da Costa Filho, C. A., M. Ravasi, A. Curtis, and G. A. Meles, 2014, Elastodynamic Green's function retrieval through single-sided Marchenko inverse scattering: Physical Review E, **90**, no. 6, 063201.

Farmer, P. A., I. F. Jones, H. Zhou, R. I. Bloor, and M. C. Goodwin, 2006, Application of reverse time migration to complex imaging problems: First Break, **24**.

Fink, M., 1992, Time reversal of ultrasonic fields. i. basic principles: IEEE transactions on ultrasonics, ferroelectrics, and frequency control, **39**, 555–566.

——, 1999, Time-reversed acoustics: Scientific American, **281**, 91–97.

——, 2008, Time-reversal waves and super resolution: Journal of Physics: Conference Series, **124**, 012004.

Galetti, E., and A. Curtis, 2012, Generalised receiver functions and seismic interferometry:

Tectonophysics, **532**, 1–26.

Guitton, A., A. Valenciano, and D. Bevc, 2006, Robust imaging condition for shotprofile migration: SEG Technical Program Expanded Abstracts, **506**, 2519–2523.

Hornby, B. E., and J. Yu, 2007, Interferometric imaging of a salt flank using walkaway vsp data: The Leading Edge, **26**, 760–763.

Jin, S., S. Xu, and D. Walraven, 2006, One-return wave equation migration: Imaging of duplex waves, *in* SEG Technical Program Expanded Abstracts 2006: Society of Exploration Geophysicists, 2338–2342.

Larmat, C., J.-P. Montagner, M. Fink, Y. Capdeville, A. Tourin, and E. Clévédé, 2006, Time-reversal imaging of seismic sources and application to the great sumatra earthquake: Geophysical Research Letters, **33**.

Lellouch, A., and E. Landa, 2018, Seismic velocity estimation using time-reversal focusing velocity estimation: Geophysics, **83**, U43.

Li, Y., Y. Agnihotri, and T. Dy, 2011, Prismatic wave imaging with dual flood rtm, *in* SEG Technical Program Expanded Abstracts: Society of Exploration Geophysicists, 3290–3294.

Liu, F., G. Zhang, S. A. Morton, and J. P. Leveille, 2011, An effective imaging condition for reverse-time migration using wavefield decomposition: Geophysics, **76**, S29–S39.

Löer, K., G. A. Meles, and A. Curtis, 2015, Automatic identification of multiply diffracted waves and their ordered scattering paths: The Journal of the Acoustical Society of America, **137**, 1834–1845.

Lomas, A., S. Singh, and A. Curtis, 2018, Marchenko imaging of both vertical and horizontal interfaces using vsp data, *in* SEG Technical Program Expanded Abstracts 2018: Society of Exploration Geophysicists.

Malcolm, A., B. Ursin, and V. Maarten, 2009, Seismic imaging and illumination with internal multiples: Geophysical Journal International, **176**, 847–864.

Marmalyevskyy, N., Y. Roganov, Z. Gornyak, A. Kostyukevych, and V. Mershchiy, 2005, Migration of duplex waves, *in* SEG Technical Program Expanded Abstracts 2005: Society of Exploration Geophysicists, 2025–2028.

McMechan, G. A., 1989, A review of seismic acoustic imaging by reverse-time migration:

International Journal of Imaging Systems and Technology, **1**, 18–21.

Meles, G. A., and A. Curtis, 2014, Fingerprinting ordered diffractions in multiply diffracted waves: Geophysical Journal International, **198**, 1701–1713.

Meles, G. A., K. Löer, M. Ravasi, A. Curtis, and C. A. da Costa Filho, 2014, Internal multiple prediction and removal using marchenko autofocusing and seismic interferometry: Geophysics, **80**, A7–A11.

Noble, M., J. Lindgren, A. Tarantola, et al., 1991, Large-sized nonlinear inversion of a marine data set: Retrieving the source, the background velocity and the impedance contrasts: 61st SEG meeting, Houston, USA, Expanded Abstracts, 893–896.

Pratt, W., 2013, Introduction to digital image processing: Taylor & Francis.

Rose, J., 2002, Single-sided autofocusing of sound in layered materials: Inverse problems, **18**, 1923–1934.

Sava, P., and B. Biondi, 2004, Wave-equation migration velocity analysis. I. theory: Geophysical Prospecting, **52**.

Shustak, M., and E. Landa, 2018, Time reversal for wave refocusing and scatterer detection using machine learning: GEOPHYSICS, **83**, T257–T263.

Singh, S., and R. Snieder, 2017, Strategies for imaging with Marchenko-retrieved Greens functions: Geophysics, **Vol 82(4)**, Q23–Q37.

Singh, S., R. Snieder, J. Behura, J. van der Neut, K. Wapenaar, and E. Slob, 2015, Marchenko imaging: Imaging with primaries, internal multiples, and free-surface multiples: Geophysics, **80(5)**, S165–S174.

Singh, S., R. Snieder, J. Behura, J. van Der Neut, K. Wapenaar, E. Slob, et al., 2014, Autofocusing imaging: Imaging with primaries, internal multiples and free-surface multiples: Presented at the 2014 SEG Annual Meeting, Society of Exploration Geophysicists.

Singh, S., R. Snieder, J. Thorbecke, J. van der Neut, K. Wapenaar, and E. Slob, 2016, Accounting for free surface multiples in Marchenko imaging: Geophysics, **82(1)**, R19–R30.

Slob, E., K. Wapenaar, F. Broggini, and R. Snieder, 2014, Seismic reflector imaging using internal multiples with Marchenko-type equations: Geophysics, **79(2)**, S63–S76.

Symes, W. W., and J. J. Carazzone, 1991, Velocity inversion by differential semblance

optimization: Geophysics, **56**, 654–663.

Van Manen, D.-J., 2006 Chapter 4, Time-reversal and interferometry with applications to forward modeling of wave propagation and a chapter on receiver functions: PhD thesis, School of Geosciences, University of Edinburgh.

Versteeg, R., 1994, The marmousi experience: Velocity model determination on a synthetic complex data set: The Leading Edge, **13**, 927–936.

Wapenaar, K., J. Thorbecke, J. van der Neut, F. Broggini, E. Slob, and R. Snieder, 2014, Marchenko imaging: Geophysics, **79(3)**, WA39–WA57.

Whitmore, N. D., 1983, Iterative depth migration by backward time propagation: SEG Technical Program Expanded Abstracts, 382–385.

Wiggins, J. W., 1984, Kirchhoff integral extrapolation and migration of nonplanar data: Geophysics, **49**, 1239–1248.

Xu, S., and S. Jin, 2006, Wave equation migration of turning waves, *in* SEG Technical Program Expanded Abstracts 2006: Society of Exploration Geophysicists, 2328–2332.

Zhang, Y., and J. Sun, 2009, Practical issues of reverse time migration: True amplitude gathers, noise removal and harmonic-source encoding: Beijing International Geophysical Conference and Exposition 2009: Beijing 2009 International Geophysical Conference and Exposition, Beijing, China, 24–27 April 2009, Society of Exploration Geophysicists, 204–204.

Zhebel, O., D. Gajewski, and C. Vanelle, 2011, Localization of seismic events in 3d media by diffraction stacking: Presented at the 73rd EAGE Conference and Exhibition incorporating SPE EUROPEC.

Zuberi, M. A. H., and T. Alkhalifah, 2014, Generalized internal multiple imaging: Geophysics, **79**, S207–S216.

LIST OF FIGURES

8   a) TRMi of the step model in Figure 2(a) with free-surface multiples included in the recorded data, constructed by stacking the images of all shots. Note that amplitudes were increased and clipped in the images to visualize artifacts in the image. b) Final image of the step model in Figure 2(a), given by the sum of the RTM image in Figure 3 and the TRMi image in Figure 8(a).

9   Two-step staircase model with variable density and a constant seismic velocity of 2 km/s.

10   Final image: sum of RTM and the TRMi for the two-step model in Figure 9, without including free-surface multiples in the recorded data.

11   Final image: sum of RTM and the TRMi for the two-step model in Figure 9, including free-surface multiples in the recorded data.

12   A section of the Marmousi model (displayed as the physical quantity of impedance) with the x-direction compressed by a factor of 4 to create more steeply dipping reflectors. We refer to this modified version of the Marmousi model as the *squeezed Marmousi Model*.

13   a) RTM image of the squeezed Marmousi model in Figure 12. The high-impedance, steeply dipping faults picked from the model in Figure 12 are outlined by red dots. b) TRMi of the squeezed Marmousi model in Figure 12 using the same reflection data as was used to construct the RTM image in Figure 13(a). Red dots are the same as in Figure 13(a). c) Final image of the model in Figure 12: Image = RTM in (a) + TRMi in (b).

14   a) RTM image of a squeezed Marmousi model similar to Figure 12 but with the contrast in impedance determined by velocity heterogeneity with constant density of 2 kg/m^3, and a smooth reference model. b) Associated TRMi of the model used in (a). c) Final image for this model: Image= RTM in (a) + TRMi in (b).

15   Schematic of waves that overlap to image the interface along the yellow line in Figure 14(b): the solid black line is the reflected primary while the dotted line is the transmitted diving wave. Note that to create the diving wave, we extended the smooth reference velocity model in depth past 0.6 km.

16   Final image: sum of the RTM and TRMi for the step model in Figure 2(a), using a migration reference model that is too slow (25% slower than the correct velocity). The vertical structure is imaged too deeply while the horizontal reflectors are imaged too shallowly, leaving a gap between the two.
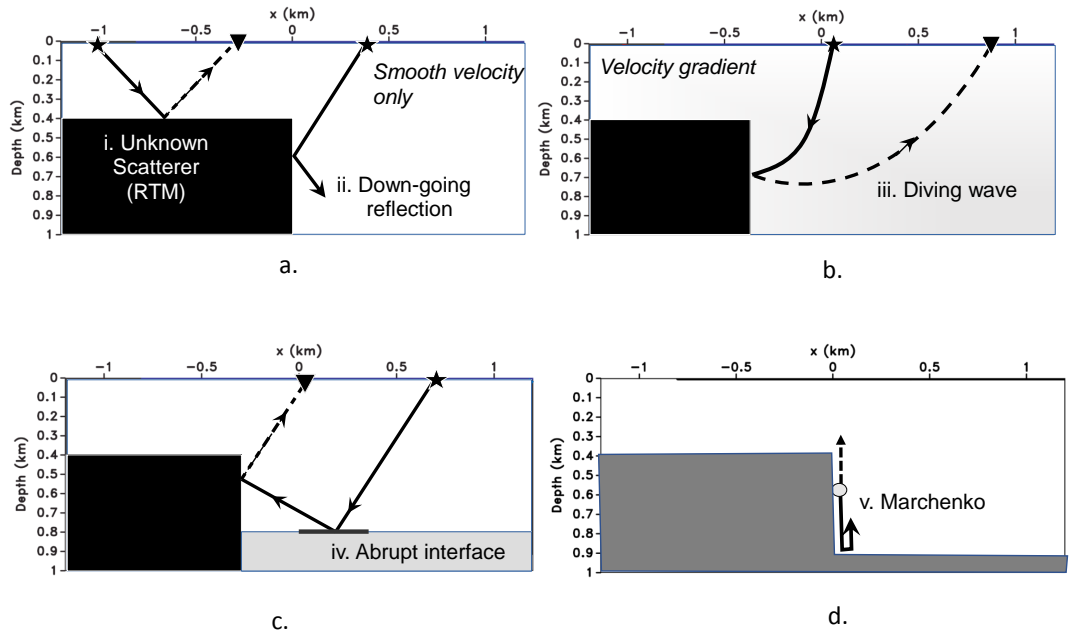
Figure 1: Schematic cartoon of different types of imaging methods with their associated reference model. We separate the various wave types and methods into 5 categories: i. primaries used in reverse-time migration (RTM) with a smooth reference model. ii. Down-going wave that cannot be extrapolated from the surface using a constant-velocity model. iii. Reflected diving waves that can be extrapolated and hence used for RTM if velocity increases correctly with depth in the smooth model. iv. Including abrupt interfaces in the reference model (solid horizontal line) can allow us to predict up-going waves from the source, which can then be used to image vertical structures. v. The up- and down-going Green's functions (dotted and solid arrows, respectively) at a point(circle) on the vertical interface are kinematically different, hence it is not possible to image the vertical structure at the interface using Marchenko imaging methods. In panels other than lower-right, solid rays would be predicted from the source side within RTM, while dashed rays would be predicted from the receiver side.
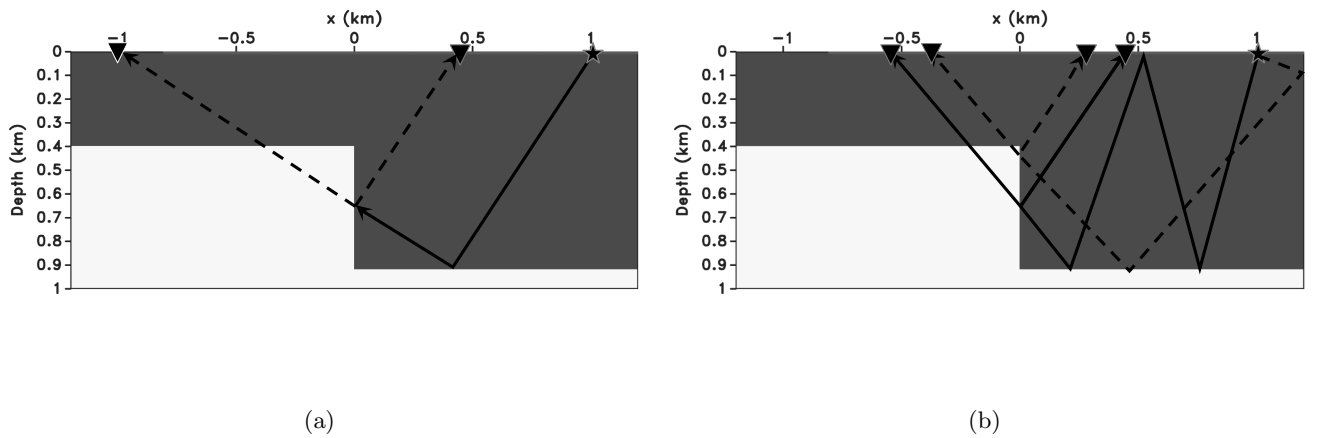
Figure 2: a) Step model and schematic of primary (left-going) and duplex (right-going) waves that we use for imaging vertical structures. The star represents a source, the solid line is the source ray path before reflecting from the vertical structure, dashed lines represent the transmitted (primary) and reflected wave (duplex) after the source ray meets the vertical structure. The rays through the step are straight because the contrast is only in the density, (our imaging scheme also works for variable velocity profiles). b) Similarly for the case of multiply scattered waves, but with solid lines for rays produced by free-surface multiples, and dashed lines for rays produced by an internal multiply scattered wave.
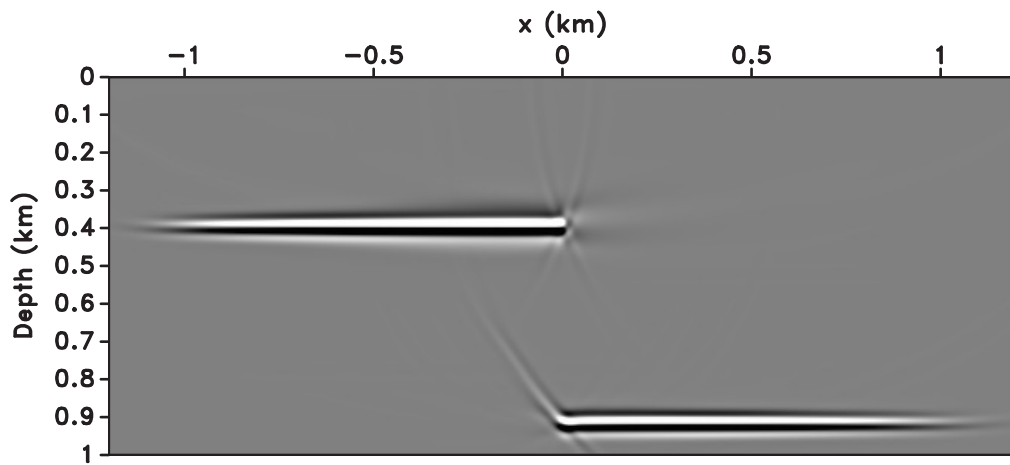
Figure 3: Reverse-time migration image of the step model in Figure 2(a).
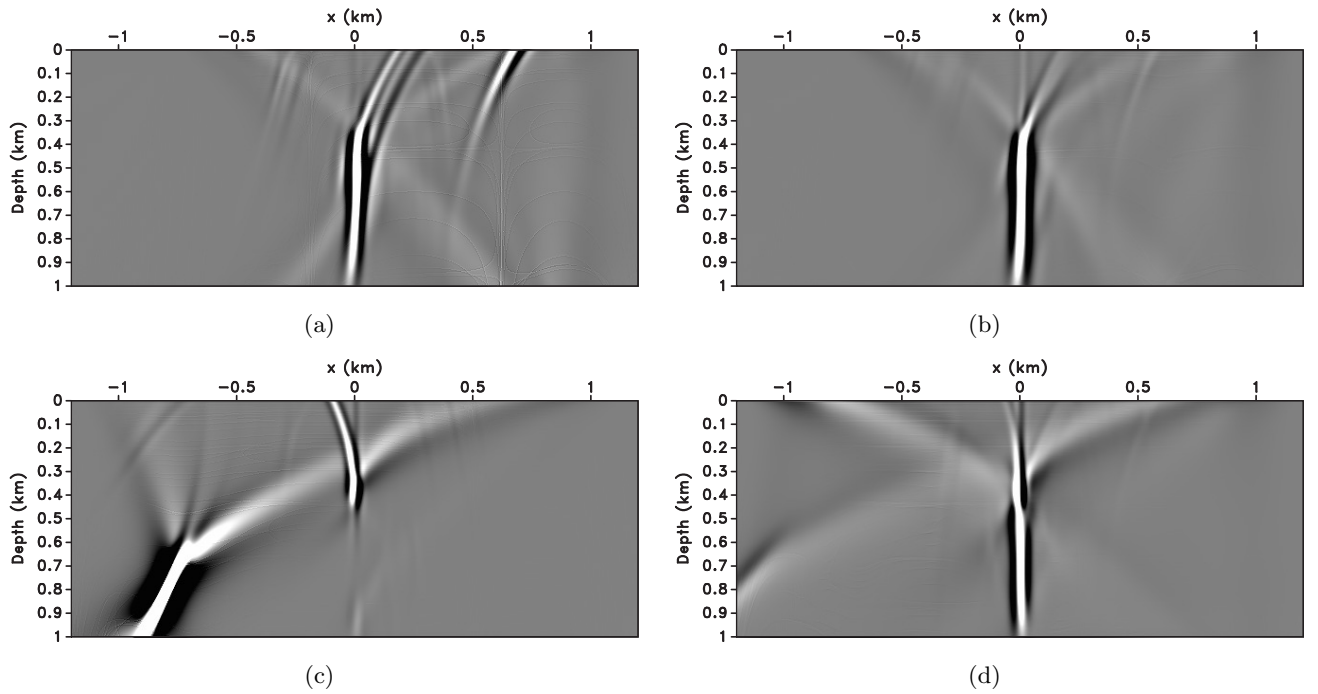
Figure 4: TRMi of the step model in Figure 2(a). a) TRMi for a single shot at x=1 km. The recorded data that is used for this image does not have free-surface multiples. b) TRMi constructed by stacking the images of all shots to the right of the vertical interface (those shots that create duplex waves). c) TRMi for a single shot at x=-1 km. We increased the gain on the amplitudes in this panel to highlight in the image the relatively low-amplitude diffractor at the bottom corner of the step compared to the other events. d) TRMi for all shots at the surface.
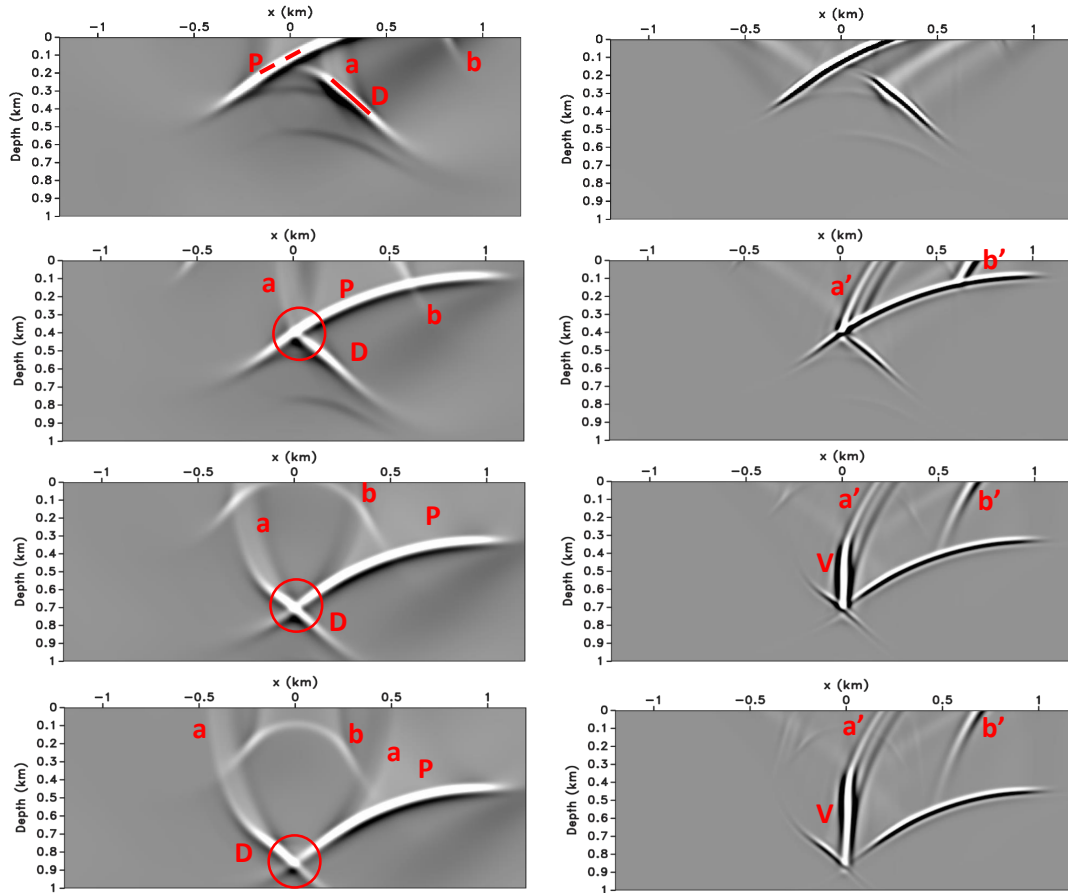
Figure 5: Snapshots of the receiver wavefield (*left column*) $U_r(x, \bar{t}_0)$, and the associated cumulative TRMi $I(x, \bar{t}_0)$ (*right column*) which includes only energy for $t \in [\bar{t}_0, T]$ for a single shot at x=1 km. Start time $\bar{t}_0$ starts at 1.2 seconds and decreases by 0.12 s in successive rows, while T is the fixed maximum recording time of 3.1 s. In the receiver wavefield (left) the events are: $\langle$a$\rangle$ edge artifact from injecting the recorded data from a finite-aperture array into a finite-difference modeling scheme. $\langle$b$\rangle$ Diffraction from top of the step at **x**=0 km. $\langle$P$\rangle$ Primary wave transmitted though the step, similar to the dashed left ray in Figure 2(a). $\langle$D$\rangle$ Duplex wave similar to the right dashed up-going wave in Figure 2(a). Areas of overlap that contribute energy to the image at the correct locations are circled. In the cumulative TRMi image (*right column*) the labeled events are: $\langle$a'$\rangle$ TRMi contribution of $\langle$a$\rangle$ and $\langle$P$\rangle$ overlapping in the receiver wavefield. $\langle$b'$\rangle$ TRMi contribution of $\langle$b$\rangle$ and $\langle$P$\rangle$ overlapping. $\langle$V$\rangle$ Image of the vertical part of the step from the TRMi contribution of $\langle$P$\rangle$ and $\langle$D$\rangle$ overlapping in the receiver wavefield.

29
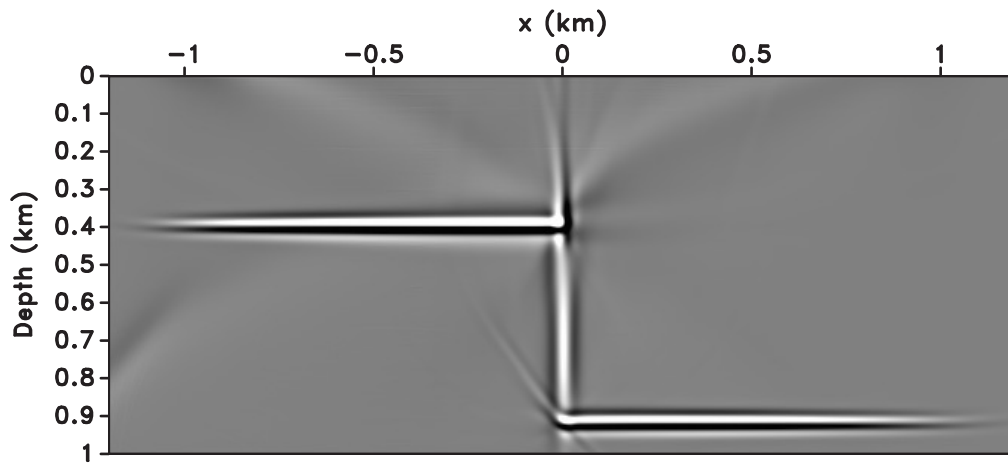
Figure 6: Final image of the step model in Figure 2(a): the sum of the RTM in Figure 3 and TRMi in Figure 4(d).
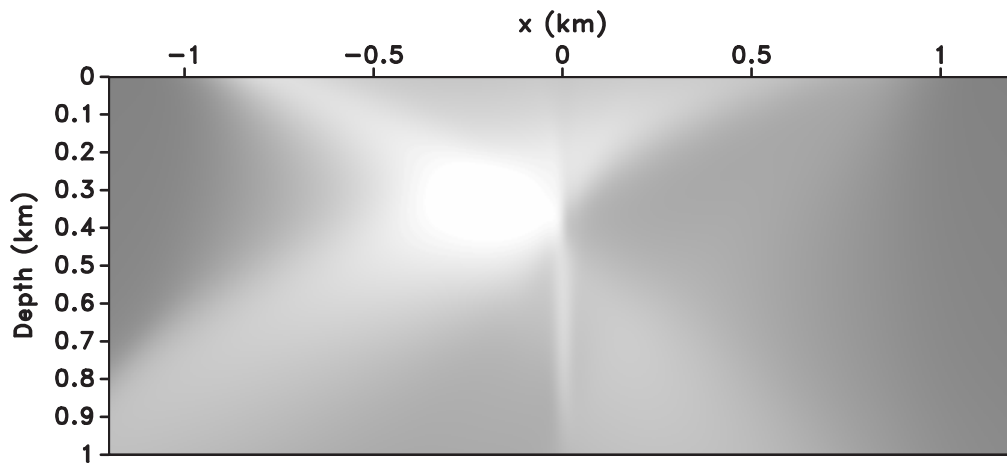
Figure 7: TRMi of the step model without including the Laplacian operator in the imaging condition, equation 2.
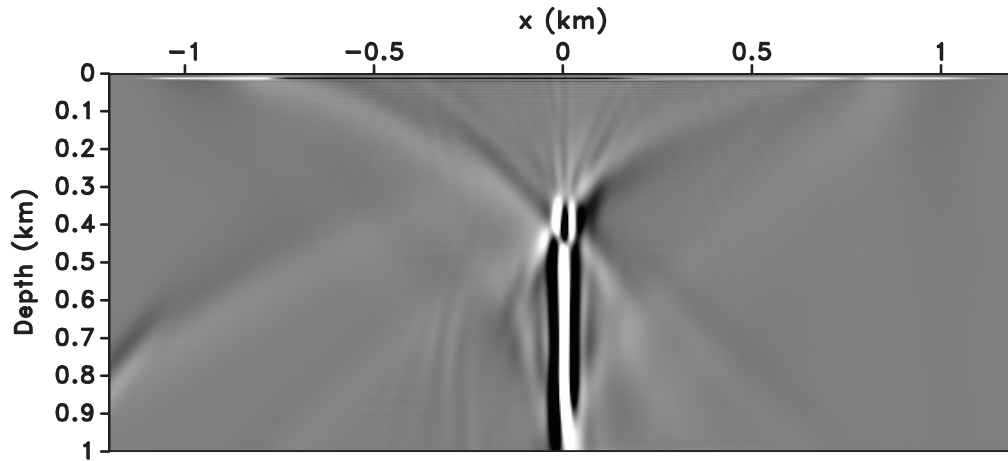
(a)
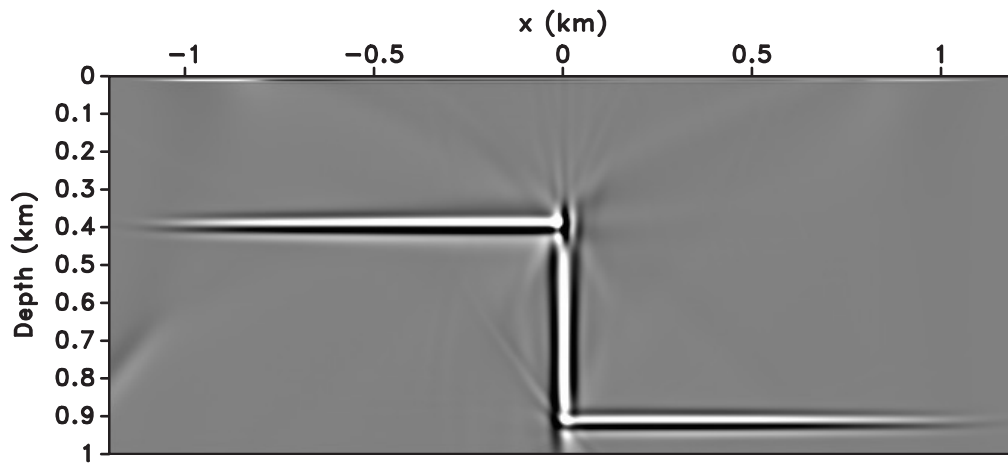
(b)

Figure 8: a) TRMi of the step model in Figure 2(a) with free-surface multiples included in the recorded data, constructed by stacking the images of all shots. Note that amplitudes were increased and clipped in the images to visualize artifacts in the image. b) Final image of the step model in Figure 2(a), given by the sum of the RTM image in Figure 3 and the TRMi image in Figure 8(a).
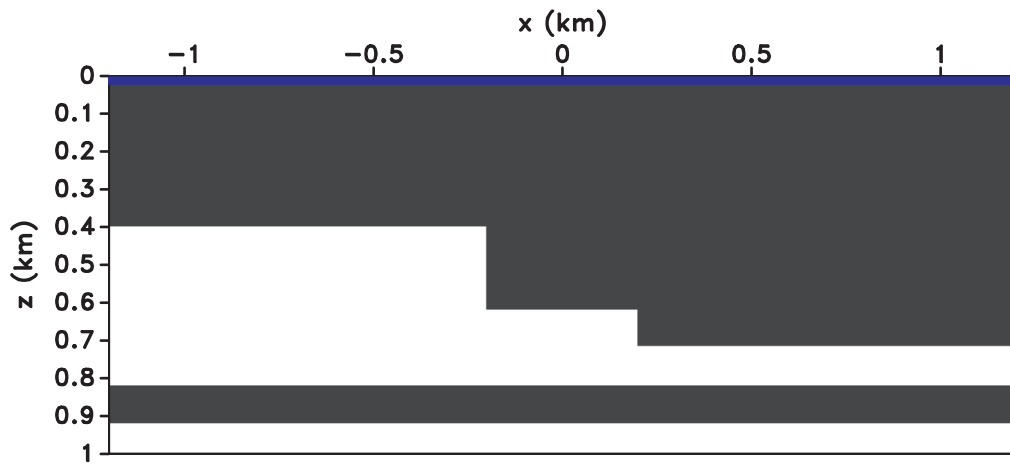
Figure 9: Two-step staircase model with variable density and a constant seismic velocity of 2 km/s.
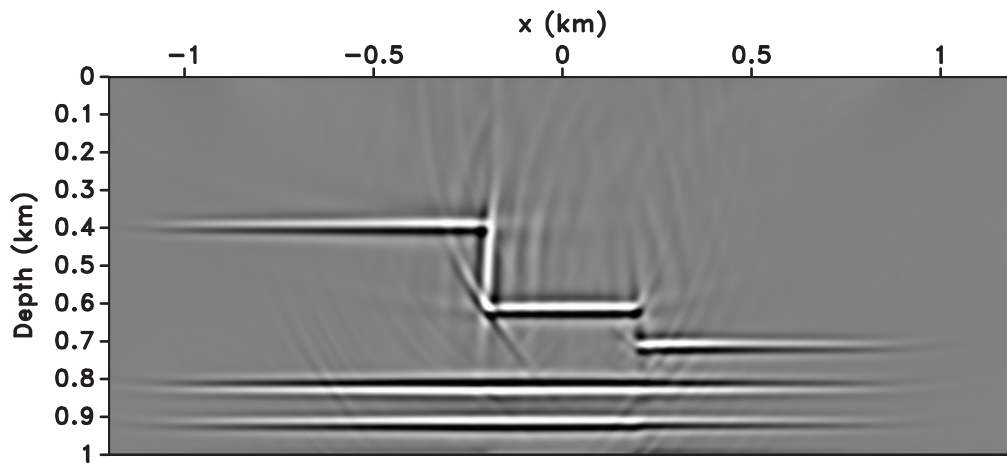
Figure 10: Final image: sum of RTM and the TRMi for the two-step model in Figure 9, without including free-surface multiples in the recorded data.
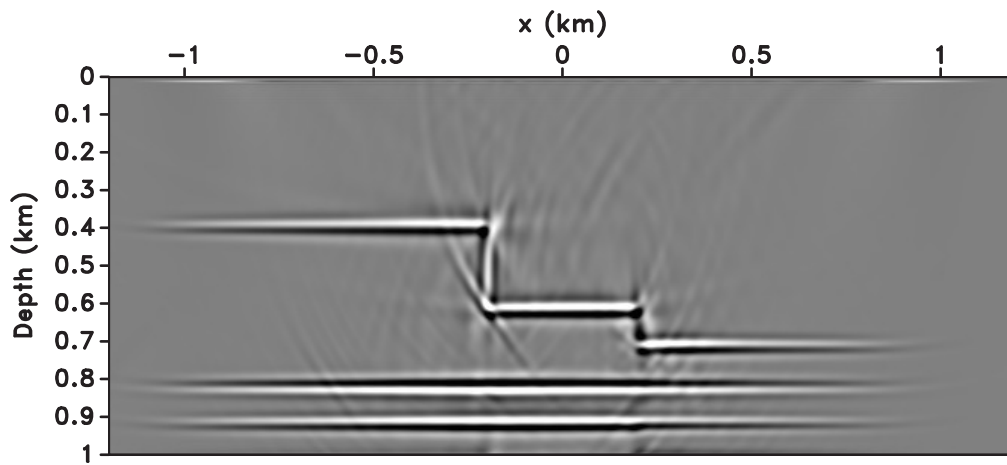
Figure 11: Final image: sum of RTM and the TRMi for the two-step model in Figure 9, including free-surface multiples in the recorded data.
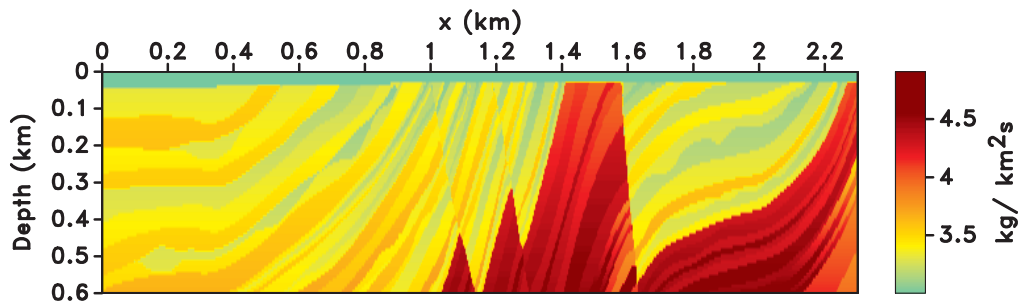
Figure 12: A section of the Marmousi model (displayed as the physical quantity of impedance) with the x-direction compressed by a factor of 4 to create more steeply dipping reflectors. We refer to this modified version of the Marmousi model as the *squeezed Marmousi Model*.
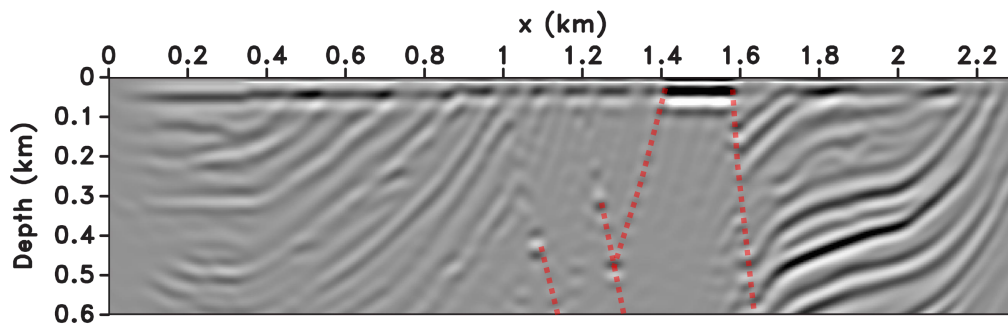
(a)
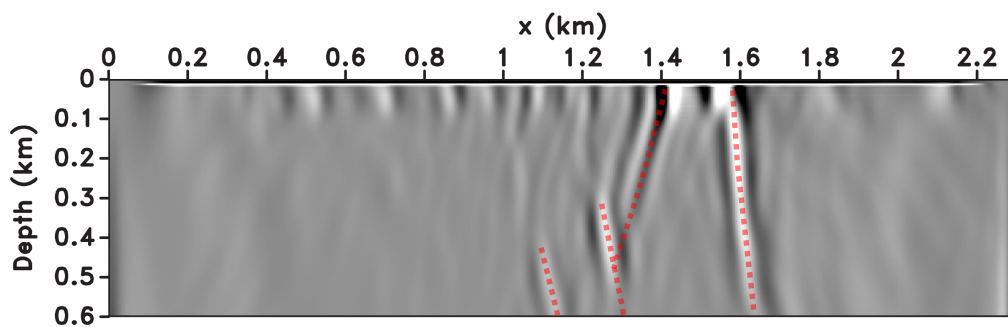
(b)
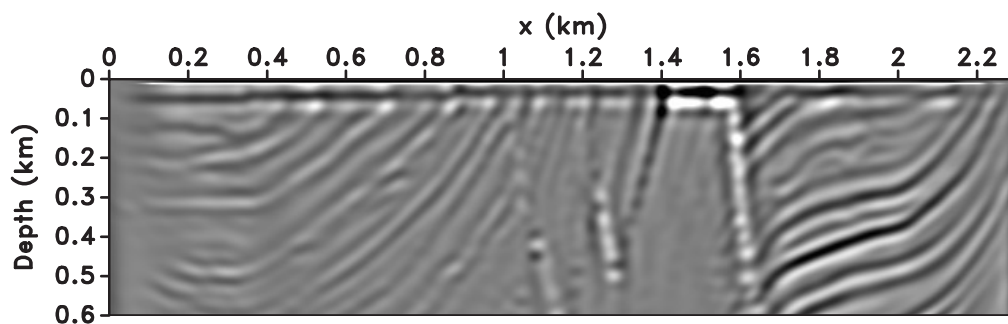
(c)

Figure 13: a) RTM image of the squeezed Marmousi model in Figure 12. The high-impedance, steeply dipping faults picked from the model in Figure 12 are outlined by red dots. b) TRMi of the squeezed Marmousi model in Figure 12 using the same reflection data as was used to construct the RTM image in Figure 13(a). Red dots are the same as in Figure 13(a). c) Final image of the model in Figure 12: Image = RTM in (a) + TRMi in (b).
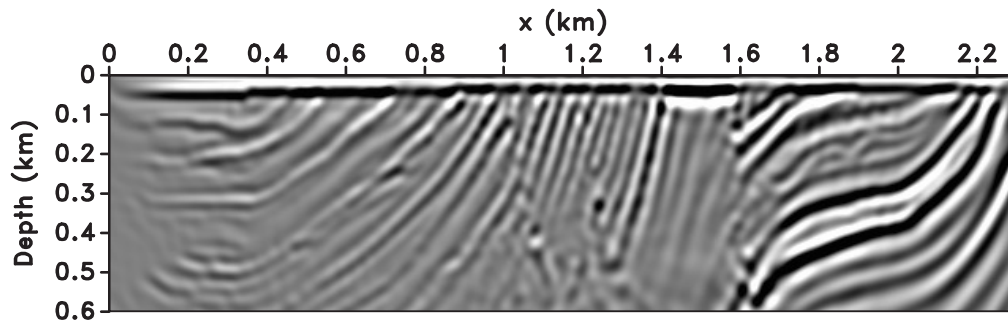
(a)
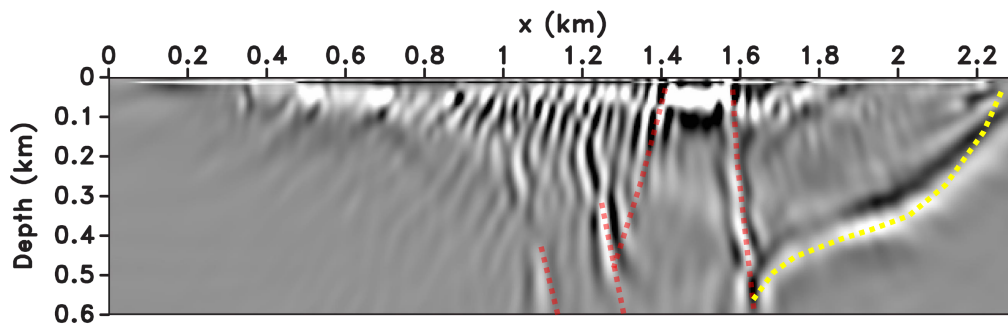
(b)
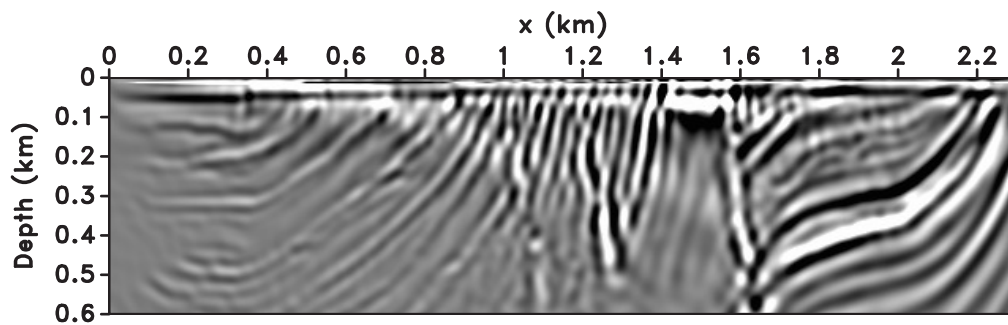
(c)

Figure 14: a) RTM image of a squeezed Marmousi model similar to Figure 12 but with the contrast in impedance determined by velocity heterogeneity with constant density of 2 kg/m^3, and a smooth reference model. b) Associated TRMi of the model used in (a). c) Final image for this model: Image= RTM in (a) + TRMi in (b).
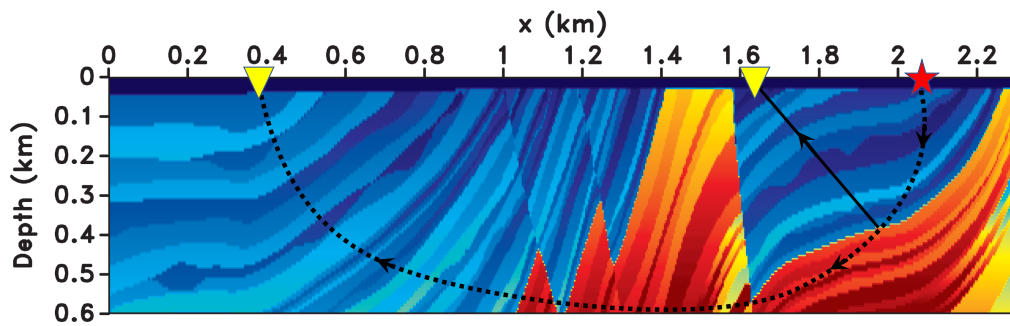
Figure 15: Schematic of waves that overlap to image the interface along the yellow line in Figure 14(b): the solid black line is the reflected primary while the dotted line is the transmitted diving wave. Note that to create the diving wave, we extended the smooth reference velocity model in depth past 0.6 km.
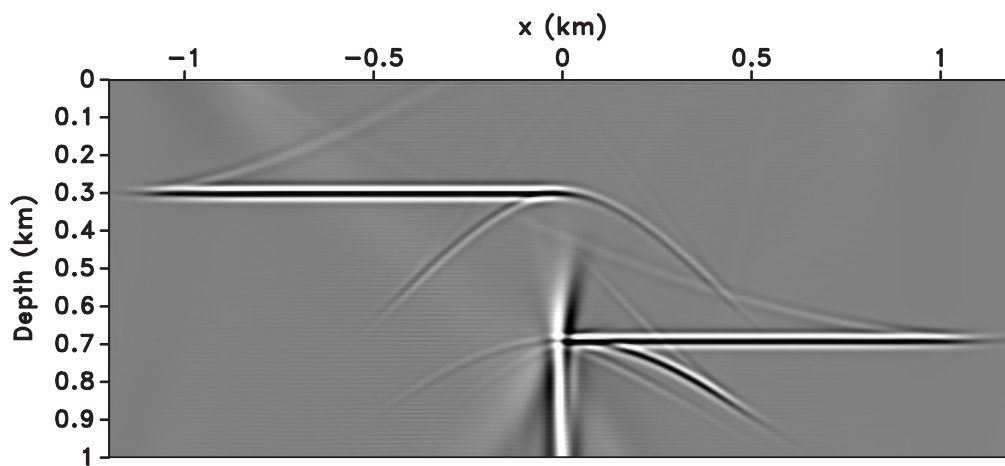
Figure 16: Final image: sum of the RTM and TRMi for the step model in Figure 2(a), using a migration reference model that is too slow (25% slower than the correct velocity). The vertical structure is imaged too deeply while the horizontal reflectors are imaged too shallowly, leaving a gap between the two.